

# VORO<sub>TO</sub>: MULTISCALE TOPOLOGY OPTIMIZATION OF VORONOI STRUCTURES USING SURROGATE NEURAL NETWORKS

Rahul Kumar Padhy  
Department of Mechanical Engineering  
University of Wisconsin-Madison  
Madison, WI, USA  
rkpadhy@wisc.edu

Krishnan Suresh  
Department of Mechanical Engineering  
University of Wisconsin-Madison  
Madison, WI, USA  
ksuresh@wisc.edu

Aaditya Chandrasekhar  
Department of Mechanical Engineering  
University of Wisconsin-Madison  
Madison, WI, USA  
cs.aaditya@gmail.com

## ABSTRACT

Cellular structures found in nature exhibit remarkable properties such as high strength, high energy absorption, excellent thermal/acoustic insulation, and fluid transfusion. Many of these structures are Voronoi-like; therefore researchers have proposed Voronoi multi-scale designs for a wide variety of engineering applications. However, designing such structures can be computationally prohibitive due to the multi-scale nature of the underlying analysis and optimization. In this work, we propose the use of a neural network (NN) to carry out efficient topology optimization (TO) of multi-scale Voronoi structures. The NN is first trained using Voronoi parameters (cell site locations, thickness, orientation, and anisotropy) to predict the homogenized constitutive properties. This network is then integrated into a conventional TO framework to minimize structural compliance subject to a volume constraint. Special considerations are given for ensuring positive definiteness of the constitutive matrix and promoting macroscale connectivity. Several numerical examples are provided to showcase the proposed method.

**Keywords** Topology Optimization · Voronoi Structures · Neural Network

## 1 INTRODUCTION

Topology optimization is a powerful engineering tool employed to optimize the distribution of material within a given design domain to achieve optimal performance under specified constraints [1, 2]. Traditionally, single-scale topology optimization focuses on determining the optimal layout of material within a structure at a single scale, aiming primarily at maximizing stiffness [1] for a given set of loading conditions. However, engineering applications often demand more than just structural efficiency [3]. Features such as structural robustness [4], high strength [5], superior energy absorption [6], fluid circulation [7], thermal and acoustic insulation [8] capabilities are crucial. These attributes not only enhance the overall performance of structures but also facilitate multifunctionality, making them indispensable across various industries, ranging from aerospace [9, 10], biomedical [11, 12], and more [13].

Many natural structures, such as bones [14], wood [15], and insect wings [16] exhibit remarkable combinations of strength, energy absorption, fluid circulation, and insulating properties. These features are often achieved through the intricate arrangement of porous structures, which possess desirable properties such as stochasticity [17], anisotropy [18, 19], and connectivity [20]. For instance, consider the calcaneus (heel bone) and its associated loading conditions during walking, as depicted in fig. 2. This scenario can be effectively modeled as a simple cantilever beam as in fig. 3a [19]. The growth of bone entails a

continuous self-optimization process, where its internal structure adapts to maximize mechanical efficiency under varying external conditions. This behavior can be modeled through topology optimization, by formulating the problem of maximizing stiffness [21, 19].

The heel bone topology optimization problem is idealized fig. 3a. An optimal design that maximizes stiffness using single-scale topology optimization is presented in fig. 3b. Although this design is optimal for stiffness, it lacks the porosity essential for fluid movement. In bones, pores play a vital role in blood and interstitial fluid movement, enabling the exchange of oxygen and nutrients between tissues [7]. A hypothetical porous structure that sacrifices stiffness for porosity [22, 23, 24] is depicted in fig. 3c.

Systematic computation of such structures poses significant computational challenges due to their multiscale nature [25, 26]. Theoretically, one can use high-resolution single-scale topology optimization to arrive at such structures, but this is not viable in practice [26]. Here, we present a neural network (NN) based computationally efficient multiscale topology optimization approach for computing such structures. Furthermore, we use Voronoi microstructures to represent porosity as they offer high design freedom [27], exhibit anisotropy, and often resemble the porous structures found in bone [28, 29]. A parametric representation of the microstructures is used to train an NN, facilitating the mapping of microstructure parameters to homogenized properties. Special attention is given to the parametric representation

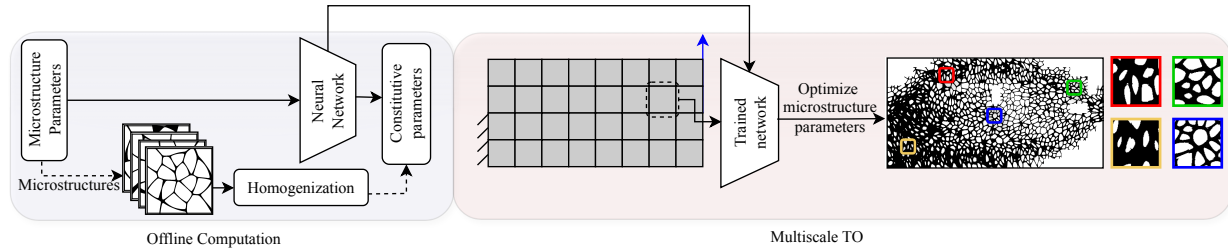


Figure 1: Graphical abstract: Offline computation: Given a dataset containing Voronoi microstructure parameters and homogenized constitutive properties, a neural network is trained offline. Multiscale TO: The trained network is used as a surrogate during topology optimization to derive optimized Voronoi structures.



Figure 2: Heel bone and loading conditions.

to promote macroscale connectivity, addressing a limitation [30] not inherently present in unit cell-based multiscale topology optimization approaches [31, 32].

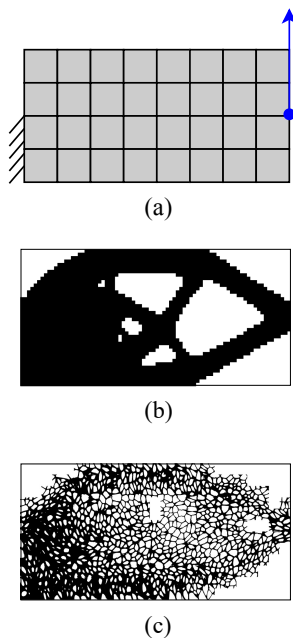


Figure 3: (a) Topology optimization problem. (b) Single scale design. (c) A multiscale porous design.

### 1.1 Topology optimization of porous structures

Topology optimization of porous structures has gained considerable attention, with two primary approaches [30]: full-scale

and multi-scale. The full-scale approach employs geometrical constraints such as pattern repetition [33, 34] and local volume constraints [35, 36, 37] to generate optimized porous structures. Recent enhancements include incorporating length scale constraint [38] and parametrized porous structures [39]. Although these approaches can generate optimized porous structures, the incorporation of additional geometrical constraints often results in reduced performance when compared to traditional topology optimization methods [40]. Furthermore, these approaches can be computationally expensive because of the need for high-resolution topology optimization of fine porous structures [26].

Multi-scale approaches separate the optimization problem into macro and micro scales, enabling customization of local material properties and macroscale structural behavior [30, 41]. It has yielded materials with exceptional properties, such as micro-modules with high Young's modulus [42]. Advanced techniques such as clustering [43] and level-set-based [44] optimization are used to enhance structural properties and to obtain designs with smooth boundaries respectively. Fixed types of parametric cells were used to design porous structures such as planar rod networks [45], or TPMS (triply periodic minimal surfaces) based [46, 47, 48]. These approaches reduce computational costs in generating foams with valid geometry but have a limited design space [49]. For a comprehensive review of these approaches, please see [30].

### 1.2 Voronoi based porous structure optimization

Traditionally, regular shapes such as diamond [50] and honeycomb [51] have been used to represent porous structures. However, these regular structures are susceptible to stress shielding and often exhibit limited permeability for fluid movement [52]. Consequently, there is growing research interest in irregular porous structures, specifically, Voronoi tessellation [53, 27], to model the complex shapes of bone structures. Voronoi tessellations offer high design freedom [27], exhibit anisotropy, and often resemble the porous structures found in nature [28, 29].

Various stochastic methods based on Voronoi tessellations have been proposed [54, 55, 26], but these lead to extensive data occupancy and are computationally intensive [56]. An alternative method involves utilizing seed positions and beam radii as design parameters, enabling them to conform to freeform shapes while maintaining geometric connectivity. However, this does not facilitate the generation of anisotropic designs [49]. Another

technique employs an iterative process of removing and adding site points to achieve a desired stress distribution on the porous structure, but it lacks the capability for optimizing a Voronoi structure through continuous sensitivity analysis [57]. A multi-scale approach was introduced for designing Voronoi-graded cellular structures for heat transfer problems. This method adapts offline computation to reduce computational expenses [58]. Nevertheless, the resulting design lacks anisotropy and has a constant Voronoi strut thickness across the entire design domain.

### 1.3 Contributions

This paper presents a novel framework for generating optimized Voronoi multiscale designs with spatially varying thickness and anisotropy. In contrast to full-scale approach for Voronoi design generation [39], we leverage a multiscale design paradigm, utilizing an offline-trained NN that maps Voronoi microstructure parameters to homogenized constitutive microstructure properties. Key contributions of this work include:

- **Design space:** We consider anisotropic Voronoi cells of varying thickness in our design space, enhancing performance [29].
- **Connectivity:** In the process of designing Voronoi microstructures, neighboring cell sites are taken into account to promote connectivity.
- **Physically valid:** We ensure that the stiffness matrix predicted by the network is positive definite, i.e., physically valid.
- **End-to-end differentiability:** Our methodology is end-to-end differentiable, enabling automated sensitivity analysis for gradient-based optimization.

## 2 PROPOSED METHOD

### 2.1 Voronoi Diagram and Structure

Our objective here is to design porous structures using Voronoi diagrams. A Voronoi diagram is a geometric structure that partitions space into regions or cells based on the proximity to a specified set of points called sites [59, 60, 61]; see fig. 4. The shape of the Voronoi cell associated with a site is only influenced by that site and nearby sites. Voronoi diagrams are valuable for representing and analyzing complex spatial relationships, making them essential in computational geometry [62, 63], modeling of porous structures [53], and design problems [39].

Using the Voronoi *diagram* as a basis, we will now define a Voronoi *structure*. Let the domain contain  $\tilde{S}$  sites (points), denoted by  $(\bar{x}_s, \bar{y}_s)$ ;  $s = 1, 2, \dots, \tilde{S}$ ; this results in  $\tilde{S}$  cells. We now associate 3 parameters with each cell: (1)  $\beta_s$  to create a thickness to the cells, (2)  $\alpha_s$  to control the degree of anisotropy, and (3)  $\theta_s$  to control the orientation. These parameters are essential to obtain an optimal distribution of porous material. The resulting Voronoi structure is defined using a density function as follows. Given any point  $(x, y)$  we define an anisotropic [64, 65] and oriented distance [66] of  $(x, y)$  to any cell site  $s$  as:

$$d_s(x, y) = \sqrt{\alpha_s(\delta_s^x)^2 + (\delta_s^y)^2/\alpha_s} \quad (1)$$

where,

$$\begin{pmatrix} \delta_s^x \\ \delta_s^y \end{pmatrix} = \begin{bmatrix} \cos \theta_s & -\sin \theta_s \\ \sin \theta_s & \cos \theta_s \end{bmatrix} \begin{pmatrix} x - \bar{x}_s \\ y - \bar{y}_s \end{pmatrix} \quad (2)$$

Then the density field associated with a site  $s$  is defined via a soft-max function [39]:

$$\hat{\rho}_s(x, y) = \left( \frac{e^{-kd_s(x, y)}}{\sum_{s=1}^{\tilde{S}} e^{-kd_s(x, y)}} \right)^{\beta_s} \quad (3)$$

where the parameter  $k$  controls the sharpness of the soft-max function [39]. Observe that  $\hat{\rho}_s(\bar{x}_s, \bar{y}_s) = 1$  when the point  $(x, y)$  is closest to site  $s$ , and approximately 0 far away from it. Finally, we can compute the total density field at  $(x, y)$  as:

$$\rho(x, y) = 1 - \sum_{s=1}^{\tilde{S}} \hat{\rho}_s(x, y) \quad (4)$$

A typical density field is illustrated in fig. 5. While the sites control the topology of the Voronoi structure, the parameters  $\beta_s$ ,  $\alpha_s$ , and  $\theta_s$  control its shape; additional examples are provided later.

### 2.2 Single Scale Voronoi Structure Optimization

In principle, one can now optimize the location of the  $\tilde{S}$  cell sites  $(\bar{x}_s, \bar{y}_s)$ , the thicknesses  $\beta_s$ , anisotropies  $\alpha_s$  and orientations  $\theta_s$  to design optimal Voronoi structures. For example, one may pose a compliance minimization problem, subject to a volume constraint as:

$$\underset{\bar{x}, \bar{y}, \beta, \theta, \alpha}{\text{minimize}} \quad J = \mathbf{f}^T \mathbf{u} \quad (5a)$$

$$\text{subject to} \quad \mathbf{K} \mathbf{u} = \mathbf{f} \quad (5b)$$

$$\text{and} \quad V \leq V^{\max} \quad (5c)$$

$$x_{\min} \leq \bar{x}_s \leq x_{\max}, \quad \forall s \quad (5d)$$

$$y_{\min} \leq \bar{y}_s \leq y_{\max}, \quad \forall s \quad (5e)$$

$$\beta_{\min} \leq \beta_s \leq \beta_{\max}, \quad \forall s \quad (5f)$$

$$\alpha_{\min} \leq \alpha_s \leq \alpha_{\max}, \quad \forall s \quad (5g)$$

$$\theta_{\min} \leq \theta_s \leq \theta_{\max}, \quad \forall s \quad (5h)$$

where  $\mathbf{K}$  is global stiffness matrix,  $\mathbf{f}$  is the applied load. For example, the authors of [39] illustrate optimizing Voronoi structures by varying cell site locations, thickness, and anisotropy to minimize compliance. However, this is computationally prohibitive for designing fine-scale porous structures since it will require a large number of cell sites  $\tilde{S}$ , but, more importantly, it will entail a dense finite element mesh to capture the thin features. In other words, a single-scale optimization is not a viable strategy for achieving porous structures. Instead, we will pursue a multi-scale framework, discussed in the next section.

### 2.3 Proposed Method: Overview

To achieve a multi-scale design, we discretize the domain into a finite number of *macro* elements, where each element  $e$  contains a small number of  $S$  cell sites,  $(\bar{x}_s^{(e)}, \bar{y}_s^{(e)})$ ;  $s = 1, 2, \dots, S$ ;

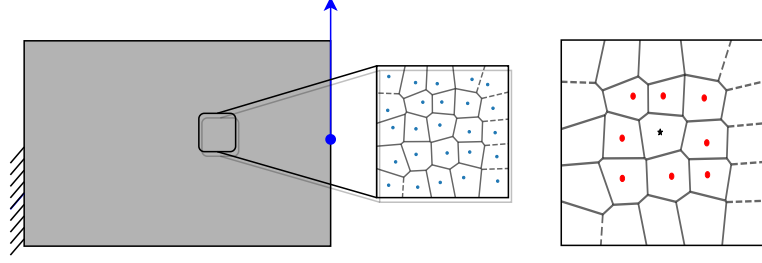


Figure 4: Voronoi diagram defined by a set of sites (points). The shape of cell (★) is influenced by its immediate neighbors (●).

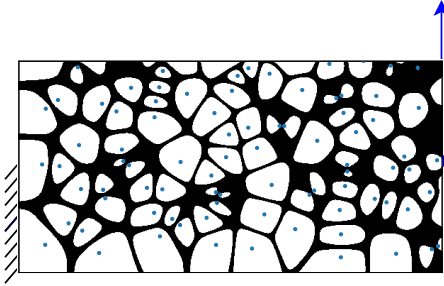


Figure 5: A typical density field defining a Voronoi structure.

$S = 4$  in this paper. Furthermore, each element will be associated with 3 additional parameters: the thickness parameter  $\beta^{(e)}$ , the anisotropy parameter  $\alpha^{(e)}$ , and the orientation parameter  $\theta^{(e)}$ . Observe that the parameters associated with an element are common to all sites within the element. By optimizing all parameters over all elements (as discussed in the remainder of the paper), one can design a multi-scale porous structure; this is schematically illustrated in fig. 6. However, direct optimization will still be computationally prohibitive due to the need for high resolution finite element analysis.

To reduce the computational cost we propose a two-stage strategy (see the graphical abstract fig. 1):

1. **Offline Computation:** This involves generating numerous representative Voronoi microstructures, computing their homogenized properties and training of NNs (see section 2.4).
2. **Multi-Scale Optimization:** Exploiting the trained NNs to carry out efficient multi-scale Voronoi structure generation (see section 2.5).

## 2.4 Offline Computation

We now describe various steps in the offline computation.

### 2.4.1 Voronoi Microstructure Generation

The first step is to create a large, representative set of Voronoi microstructures associated with the macro elements. A naive approach is to generate  $S$  random sites (points) within a macro element and generate the corresponding Voronoi microstructure. However, this would not represent a typical microstructure since points in the neighboring macro elements also influence the

Voronoi microstructure. For example, the naive approach would fail to generate solid material on the element's boundary. We therefore consider a macro element and its 8 neighboring macro elements, and generate random cell sites in all 9 elements; see fig. 7a. Then, a Voronoi microstructure is generated in the central element using all the cell sites, and a random set of parameters [67]  $\beta$ ,  $\alpha$  and  $\theta$ , that are generated uniformly over a pre-defined range, as described in numerical experiments; see fig. 7b for a typical Voronoi microstructure.

Further, to ensure that the points are sufficiently separated from one another, we model the points as a perturbation  $(\Delta_x, \Delta_y)$  from grid points; see fig. 8.

### 2.4.2 Homogenization

Once these Voronoi microstructures are generated, the macro element is discretized into a grid of  $120 \times 120$  *micro* elements; see fig. 9a. The mesh is then used for numerical homogenization to compute the elasticity matrix  $\mathbf{C}$  and the volume fraction  $v$ ; see fig. 9b and fig. 9c. Without a loss of generality, we assume a Young's Modulus  $E = 1$  and a Poisson's ratio  $\nu = 0.3$ ; see [68] for details on numerical homogenization.

### 2.4.3 Cholesky Decomposition

In the subsequent sections, we employ a NN to establish a mapping between the Voronoi parameters, and the corresponding homogenized elasticity matrix components (and volume fraction). However, a direct mapping might lead to the prediction of stiffness matrices that are not positive definite [69]. To avoid this, we first carry out a Cholesky decomposition of  $\mathbf{C}$ :

$$\mathbf{C} = \mathbf{L}\mathbf{L}^T \quad (6)$$

where,

$$\mathbf{L} = \begin{bmatrix} L_{00} & 0 & 0 \\ L_{10} & L_{11} & 0 \\ L_{20} & L_{21} & L_{22} \end{bmatrix}$$

The components of  $\mathbf{L}$ , i.e.,  $\{L_{00}, L_{10}, \dots, L_{22}\}$  are then used for training the NN, as discussed next.

### 2.4.4 Neural Network Training

Following the data generation and Cholesky decomposition, we use NNs [70] to establish a mapping between the Voronoi parameters and computed data. NNs have been utilized for various material modeling applications, including modeling the plastic

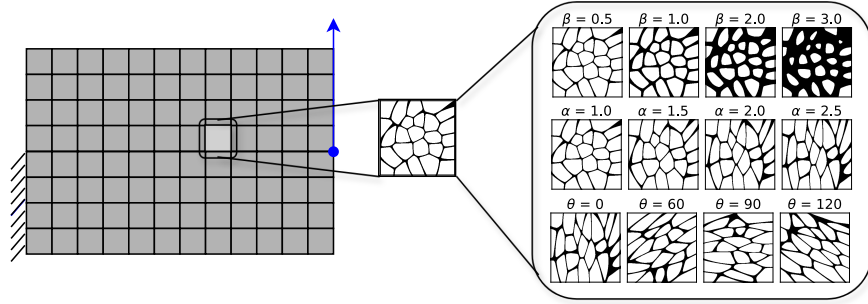


Figure 6: Given a discretized domain, we wish to populate each element with Voronoi cells. All cells in a particular microstructure have the same thickness ( $\beta$ ), and are anisotropic ( $\alpha$ ) with an orientation ( $\theta$ ).

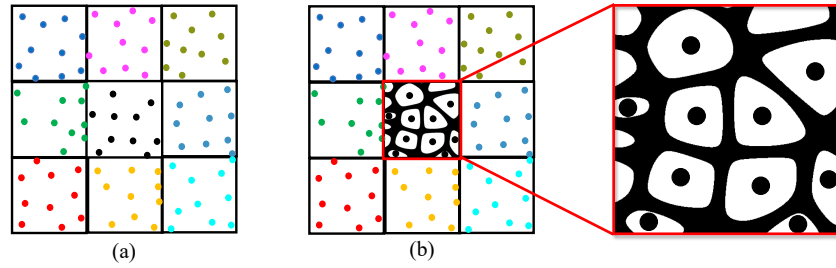


Figure 7: Data generation involves (a) distributing Voronoi cell site locations for the central microstructure element (1) and its neighbors (8), (b) generating Voronoi microstructures based on cell locations, thickness, degree of anisotropy and rotation values for the central microstructure element (c) extracting the central microstructure design.

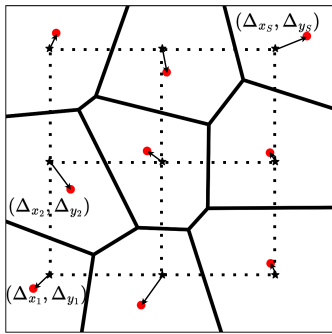


Figure 8: The cell sites ( $\bullet$ ) within a microstructure are obtained as a perturbation to a grid of points ( $\star$ ).

response of metal [71], to construct a relation between macroscopic stress and crack opening responses [72], homogenization of composite structures [73, 74], constitutive modeling of elastomeric foams [75], and nonlinear response of carbon nanotubes [76]. In addition, NNs have been utilized in the context of multi-scale topology optimization [77].

For the design of microstructures using NNs pixel-based representations have been employed [78, 79, 80]. This method assumes designs can be constructed using solid or void elements in space. While this allows extensive design flexibility, it has drawbacks [81]. There is a considerable computational burden for both design evaluation and machine learning due to limi-

tations in scalability with respect to resolution [81]. Second, efficient exploration of the design space requires the utilization of constraints to achieve desired design attributes [82]. Many studies [83, 84, 85, 86] employing NNs trained on pixel-based representations to predict microstructure properties typically optimize the networks to minimize the difference between the predicted design and a ground truth solution using loss functions such as mean squared error (MSE), mean absolute error (MAE), or binary cross-entropy. However, this approach may result in inaccurate predictions as structurally similar designs in a pixelated format can exhibit significantly different properties [81, 87].

Here, NNs are employed to predict the homogenized elastic response (and volume fraction) as a continuous and differentiable mapping of microstructure parameters, facilitating gradient-based optimization [88]. The proposed NN architecture consists of the following components (see fig. 10):

1. The input consists of the  $(x, y)$  location of the sites (points) from all 9 macro elements (the elements are ordered bottom to top, then left to right, and the parameters  $\beta$ ,  $\alpha$  and  $\theta$ , associated with the center element, i.e., the input is a  $(9 \times 2 \times S + 3)$  dimensional vector, where  $S$  is the number of cell sites per element.
2. The NN is a fully connected network consisting of four hidden layers, each comprising 50 neurons with ReLU activation functions.
3. The output layer consists the 6 components of  $\hat{\mathbf{L}}$  (the predicted values of  $\mathbf{L}$ ) and the volume fraction  $\hat{v}$  (the

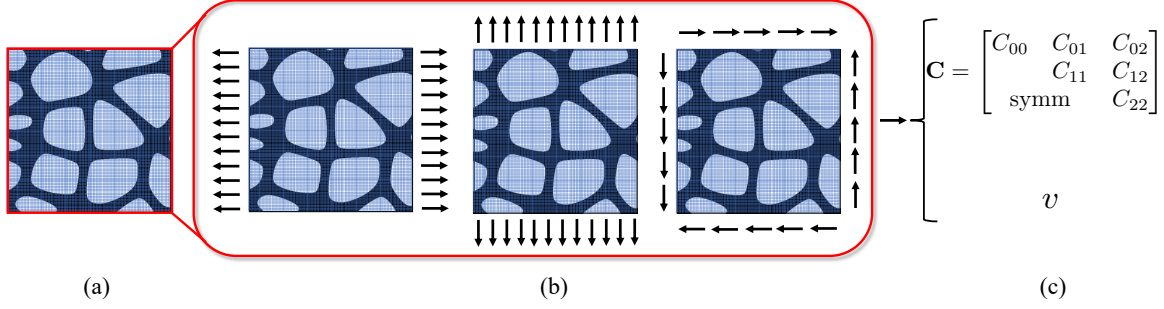


Figure 9: Numerical homogenization:(a) Discretization of the density field onto a mesh, (d) employing numerical homogenization to determine the (c) constitutive properties of the microstructure.

predicted value of  $v$ ), i.e., it is a 7 dimensional vector denoted as  $\hat{\Psi}$  (the predicted value of  $\Psi$ ). To ensure that the element stiffness matrix remains positive definite, the predicted diagonal components  $\{\hat{L}_{00}^{(e)}, \hat{L}_{11}^{(e)}, \hat{L}_{22}^{(e)}\}$  are clipped, from below, to a small positive value (of  $10^{-6}$ ).

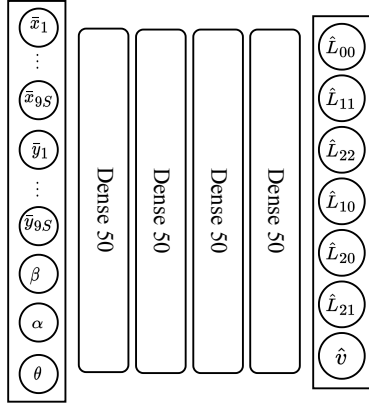


Figure 10: Proposed surrogate neural network architecture.

The NN is then trained on the ( $N_d$ ) generated data, i.e., the NN minimizes the mean squared difference between the actual and predicted microstructure properties. The loss function is defined here to be:

$$L_{NN} = \frac{1}{N_d} (\|\hat{\Psi} - \Psi\|_2^2) \quad (7)$$

## 2.5 Multi-Scale Optimization

We now consider the proposed multi-scale optimization framework illustrated in fig. 11. Recall that each macro element is associated with  $S$  cell sites and 3 geometric parameters  $\beta^{(e)}, \theta^{(e)}$  and  $\alpha^{(e)}$ . These cell sites and geometric parameters will be optimized to meet a desired objective. To avoid expensive homogenization, the trained NN can be exploited to predict the elasticity response of each element. Specifically, at each step of the optimization process, the current locations of the cell sites of  $e$  and its 8 neighbors, together with the current values

of 3 geometric parameters of  $e$  are extracted. We then apply a smoothing radial filter on the three parameters, i.e., at each element, a weighted average of every parameter about the neighborhood of that element is computed. This filtering process helps promote connectivity by smoothing out abrupt changes across neighboring microstructures.

Using these smoothed parameters, the trained NN is used to estimate  $\hat{\mathbf{L}}^{(e)}$ , and therefore  $\hat{\mathbf{C}}^{(e)}$ . Given the elasticity matrix  $\hat{\mathbf{C}}^{(e)}$  of a macro element, recall that the element stiffness matrix is defined as [89]:

$$[\mathbf{K}^{(e)}] = \int_{\Omega^{(e)}} [\nabla \mathbf{N}^{(e)}]^T [\hat{\mathbf{C}}^{(e)}] [\nabla \mathbf{N}^{(e)}] d\Omega^{(e)} \quad (8)$$

where  $[\nabla \mathbf{N}^{(e)}]$  is the gradient of the shape matrix. Once the element stiffness matrices are computed, the global stiffness matrix  $\mathbf{K}$  and force vector  $\mathbf{f}$  are assembled, followed by the solution of the displacement field  $\mathbf{u} = \mathbf{K}^{-1} \mathbf{f}$ . The objective, etc, are then computed followed by an update of all design parameters. These steps are discussed in detail in the remainder of this section.

### 2.5.1 Optimization Problem

We now describe the multi-scale optimization formulation.

**Design Variables:** The design variables for each element are represented by  $\zeta^{(e)} = \{\Delta_x^{(e)}, \Delta_y^{(e)}, \beta^{(e)}, \alpha^{(e)}, \theta^{(e)}\}$ . The complete set of design variables is represented as  $\bar{\zeta} = \{\zeta^{(1)}, \zeta^{(2)}, \dots, \zeta^{(n)}\}$ , where  $n$  is the number of macro elements.

**Objective:** We consider a simple compliance minimization objective:

$$J(\bar{\zeta}) = \mathbf{f}^T \mathbf{u} \quad (9)$$

where  $\mathbf{u}$  the nodal displacements, and  $\mathbf{f}$  is the imposed load.

**Volume Constraint:** A global volume constraint is imposed:

$$g_V(\bar{\zeta}) \equiv \frac{1}{n} \sum_{e=1}^n \hat{v}^{(e)} - v_{max} \leq 0 \quad (10)$$

where  $\hat{v}^{(e)}$  is the predicted volume fraction, and  $v_{max}$  is the imposed upper bound on the global volume fraction.

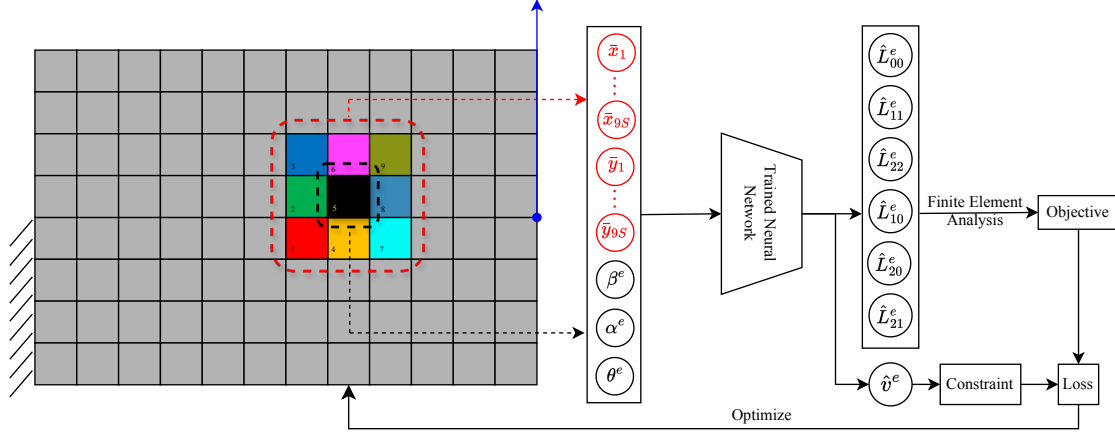


Figure 11: The multiscale topology optimization framework utilizes the cell site locations of the microstructure and its neighboring microstructures, along with the microstructure’s thickness, degree of anisotropy, and orientation to predict the constitutive properties. This prediction is achieved using the trained neural networks, facilitating finite element analysis in multiscale optimization. Note: Each microstructure element comprises  $S$  sites, and for a neighborhood of 9 elements, the neural network is provided with an input of  $9S$  sites.

Consequently, the optimization problem can be formulated as follows:

$$\underset{\bar{\zeta}=\{\zeta_1, \zeta_2, \dots, \zeta_n\}}{\text{minimize}} \quad J(\bar{\zeta}) = \mathbf{f}^T \mathbf{u} \quad (11a)$$

$$\text{subject to} \quad \mathbf{K}(\bar{\zeta})\mathbf{u} = \mathbf{f} \quad (11b)$$

$$\text{and} \quad g_v(\bar{\zeta}) \equiv \frac{\sum_{e=1}^n \hat{v}^{(e)}}{nv_{max}} - 1 \leq 0 \quad (11c)$$

$$(11d)$$

### 2.5.2 Loss Function

The constrained minimization problem eq. (11) is transformed into an unconstrained loss function minimization, using the penalty scheme [90]. Specifically, the loss function is defined as:

$$\mathcal{L}(\zeta) = \frac{J(\zeta)}{J^0} + \gamma g_v(\zeta)^2 \quad (12)$$

where  $J^0$  is the initial compliance. The constraint penalty parameter  $\gamma$  begins with an initial value of  $\gamma = 0.1$  and is subsequently incremented by  $\Delta\gamma = 0.25$  after each epoch. The gradient-based Adam optimizer [91] is used to minimize eq. (12).

### 2.5.3 Sensitivity

A critical aspect of gradient-based optimization is determining the sensitivity, or derivatives, of both the objective function and constraints with respect to the optimization parameters. Here, we harness the automatic differentiation (AD) capabilities of the PyTorch framework [92] to avoid manual sensitivity calculations [93]. In practical terms, we only need to define the forward expressions, and PyTorch’s computational library will compute all necessary derivatives with machine precision [94].

## 3 NUMERICAL EXPERIMENTS

In this section, we conduct several experiments to illustrate the method. Without loss of generality, the default parameters are as follows:

1. We assume the domain to consist of  $40 \times 20$  elements, where each element is assumed to be of unit area.
2. The material is assumed to have Young’s modulus of 1 and Poisson’s ratio of 0.3.
3. The force is assumed to be 1 unit.
4. Termination criteria include an optimization loss tolerance of  $10^{-3}$  or a maximum of 300 iterations.
5. All experiments were conducted on a MacBook M2 Air with 16 GB RAM.

Other parameters are provided in the corresponding section.

### 3.1 Offline Experiments

#### 3.1.1 Dataset Generation

To establish a mapping between microstructure element parameters and microstructure properties using a surrogate NN, the first step involves acquiring training data. This process entails allowing the 4 seed points per microstructure element  $(\bar{x}, \bar{y})$  to be uniformly distributed within a unit-length element. This distribution is achieved by varying the perturbation from the base grid points  $(\Delta_x, \Delta_y)$  within the range of  $[-0.225, 0.225]$ , ensuring a minimum separation of 0.1 between neighboring cell sites.

Additionally, the parameters thickness ( $\beta$ ), anisotropy ( $\alpha$ ) and orientation ( $\theta$ ) are considered to be in range  $[0.3, 3]$ ,  $[1, 3.5]$  and  $[0, \pi]$  respectively. These ranges are chosen to encompass a wide variation of volume fractions observed across 12000 samples of microstructure elements (as depicted in fig. 12 (a)) and to account for anisotropic homogenized elasticity matrix (as shown

in fig. 12 (b)). The thickness ( $\beta$ ), anisotropy ( $\alpha$ ) and orientation ( $\theta$ ) were filtered using a filter radius of 3.

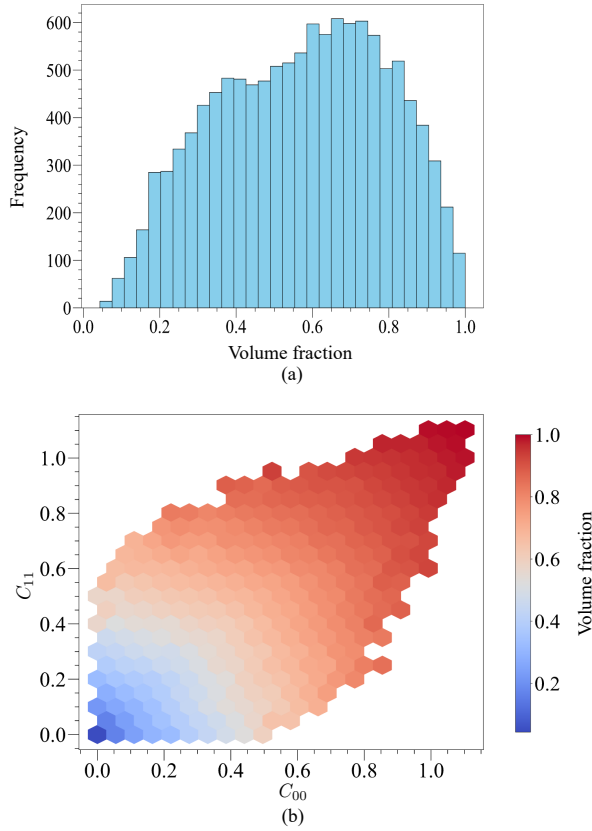


Figure 12: Distribution of (a) volume fraction and (b) constitutive matrix components  $C_{00}$  and  $C_{11}$  as a function of microstructure density.

### 3.1.2 NN Training

The training data generated in the previous section serves as input for the surrogate NN, which consists of an architecture outlined in section 2.4.4. The network’s output comprises the microstructure volume fraction and Cholesky factors of the homogenized elasticity matrix. The data is split into three sets: training ( $N_d = 10000$  data points), validation (1000 data points), and testing (1000 data points). During training, the NN aims to minimize the mean squared error between its predicted and actual microstructure properties. This training process is performed for a maximum of 300 iterations, with a learning rate of  $5 * 10^{-5}$  and a batch size of 64. The training process is stopped at the maximum iteration number or when the validation loss starts to increase, thus preventing over-fitting. Following this approach, we observe convergence in training, test, and validation loss between actual and predicted volume fraction and homogenized elasticity matrix, as depicted in fig. 13.

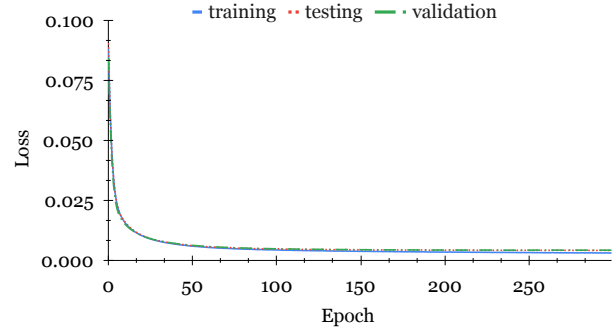


Figure 13: Convergence of the training, testing, and validation loss.

## 3.2 Multi-Scale Optimization Experiments

Next, we demonstrate multi-scale optimization through several experiments.

### 3.2.1 Validation: Tensile Bar

Consider the tensile bar problem in fig. 14(a). The objective is to find the optimal topology that minimizes compliance subjected to a volume fraction  $\nu = 0.4$  as described in [89]. The compliance of single-scale optimized design reported in reference [89] is 183. Here, we obtain a multiscale optimized design, illustrated in fig. 15 (c). As one can observe the porous structure resembles an ideal tensile bar, while meeting the minimum porosity imposed (via the parameter  $\beta$ ). Furthermore, near the transition, the porous structures are oriented along the axis, as expected. The compliance of the porous structure is 209.

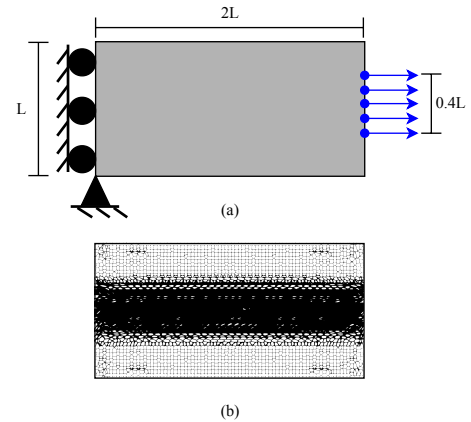


Figure 14: Validation of the multiscale framework: (a) tensile bar boundary conditions, (b) multiscale design [89] and (c) multiscale porous design.

### 3.2.2 Comparison

Next consider the mid-cantilever problem in fig. 15(a). The objective is to find the optimal topology that minimizes compliance subject to a volume fraction  $\nu = 0.6$ . The single-scale optimized design achieved using the code from [95] is illustrated in fig. 15(b); the final compliance is 61.05. In [96], by

imposing a local volume constraint of  $v = 0.6$ , an optimized porous structure with compliance of 76.86 was reported. Here, we obtain a multiscale optimized design, illustrated in fig. 15 (c), with a compliance of 68.3. The computation took 13.7 seconds. Once again, the computed structure resembles the single-scale structure but deviates from it to meet the porosity constraints.

To evaluate the accuracy of the NN mapping, we reconstructed the microstructures of the optimized design. We then computed the actual homogenized matrices via FEA of each macro element. Subsequent global analysis yielded a compliance of 74.6 and a volume fraction of 0.65. This translates to an error of 8.4% and 6.1% for the compliance and volume fraction, respectively.

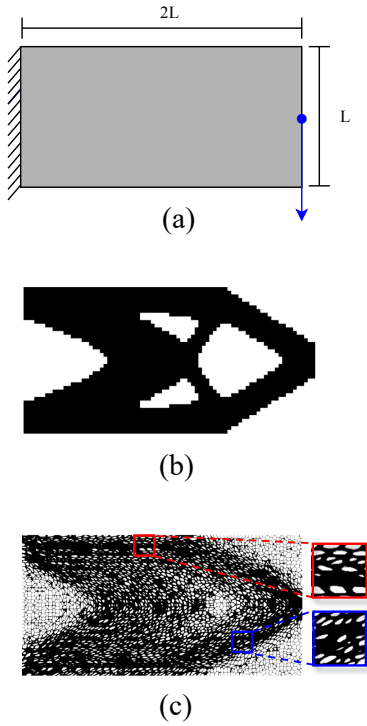


Figure 15: Validation of the multiscale framework: (a) mid cantilever boundary conditions, (b) single scale design and (c) multiscale porous design.

### 3.2.3 Convergence against Single-Scale

We illustrate the typical convergence of the proposed algorithm for the mid-cantilever problem in fig. 15(a). The compliance and volume constraint is illustrated in fig. 16. Similar convergence behavior was observed for all other examples.

### 3.2.4 Parameter Variations

A central hypothesis of our current work is that better multiscale designs can be obtained with a broader range of parameters: thickness, anisotropy, and orientation. To validate these hypotheses, we revisit the problem depicted in fig. 15(a), enforcing a volume constraint of 0.5 but considering various restrictions on the parameters.

#### Thickness Parameter: $\beta$

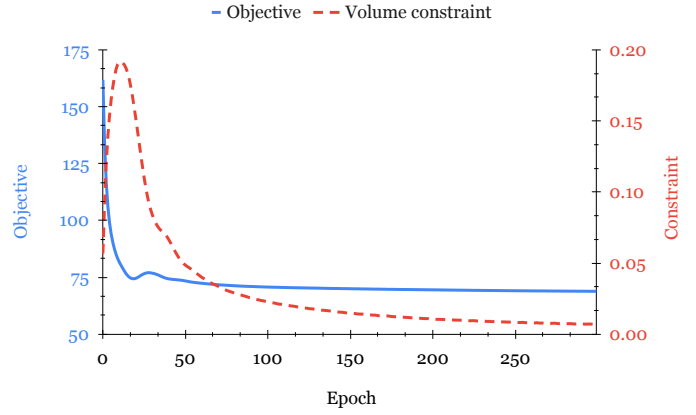


Figure 16: Convergence of the objective and constraint during optimization.

In this numerical experiment, we set the lower bound of the thickness parameter at 0.3 and analyze the impact of thickness on both the objective function and computational time by setting its upper bound to 1., 2., and 3.. The resulting topologies, illustrated in fig. 17, confirm our expectations: the objective function improves with an increasing range of thickness parameters. Furthermore, the computational time was approximately 13.7s, regardless of the range of thickness parameter.

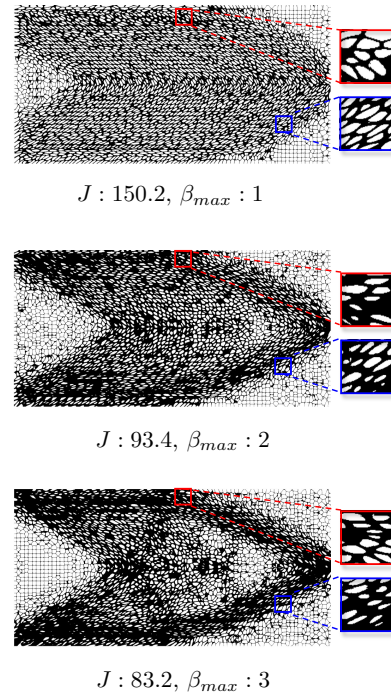


Figure 17: Impact of thickness parameter on compliance.

#### Anisotropy Parameter: $\alpha$

In this numerical experiment, we set the lower bound for the degree of anisotropy at 1 and investigate the influence of anisotropy on both the objective function and computational time by setting its upper bound to 1.5, 2.5, and 3.5. The resulting topolo-

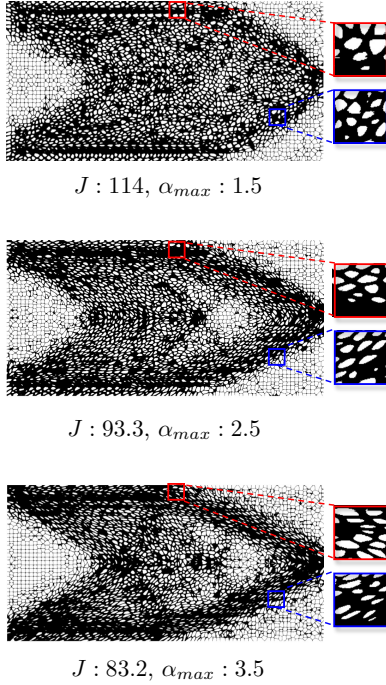


Figure 18: Varying maximum degree of anisotropy with minimum degree of anisotropy = 1

gies, as depicted in fig. 18, align with our anticipated outcomes: the objective decreases with increasing maximum degrees of anisotropy. Once again, the computational time was unaffected by the change in upper bound.

#### Orientation Parameter: $\theta$

Next, we kept the orientation fixed at  $\theta = 0$  and optimized the design. As expected, our observations, fixing the orientation results in lower performance as seen in fig. 19.

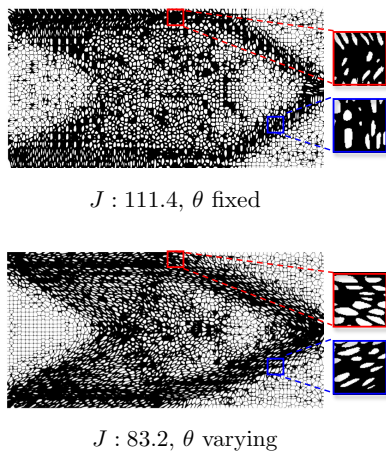


Figure 19: Impact of orientation on compliance.

#### Volume Fraction Variation

Finally, we consider the trade-off between the objective (compliance) and constraint (volume fraction) through exploration of the Pareto front is crucial for making informed design choices. In this study, we examined the heel bone problem depicted in fig. 3 (a). We determined the optimal topologies for various volume fraction constraints. The results are illustrated in fig. 20; as expected, the compliance increases as the volume fraction decreases. To evaluate the accuracy of the NN mapping, we recomputed the actual values using a macroscale FEA/ homogenization approach. The error in compliance and volume fraction was less than 10% in all cases.

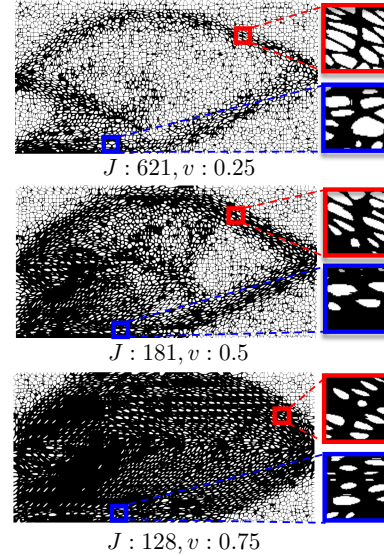


Figure 20: Trade-off between compliance and volume fraction.

#### 3.3 Is Offline Computation Justified?

The offline homogenization and data generation of 12000 microstructures required 26.4 minutes, while the training of the surrogate NN required 2 minutes. Thus, the total one-time overhead amounted to 28.4 minutes. Subsequently, the optimization of the mid-cantilever, for example, (using a grid size of  $40 \times 20$ ) consumed 0.24 minutes.

Now, let's consider two hypothetical scenarios. The first scenario is a brute-force fine-scale optimization. We note that the grid size of  $40 \times 40$  microscale elements is required for each homogenization of the microstructure element. For the single-scale optimization of the mid-cantilever (using a grid size of  $40 \times 20$  of microstructure elements), one requires a grid of  $40 \times 40 \times 40 \times 20$ , which is  $1600 \times 800$  elements. One iteration of single-scale optimization with  $1600 \times 800$  elements takes 16.62 minutes. Consequently, the anticipated total optimization time amounts to  $16.62 \times 300$ , equating to 4986 minutes.

Next, consider a scenario where we carry out multiscale optimization but do not rely on offline training, i.e., we carry out concurrent homogenization-based multiscale optimization. Observe that the time required for each homogenization is  $26.4/12000$ , i.e., 0.132 seconds. Now, for concurrent homogenization of the mid-cantilever, the task entails homogenization across every element within a  $40 \times 20$  grid over 300 iterations. As a

result, the projected optimization duration can be estimated as  $0.132 \times 800 \times 300/60$ , which equals 528 minutes.

Thus, the proposed offline NN-based multiscale optimization is computationally far superior. Furthermore, the loss in accuracy in predicted compliance and volume fraction was found to be less than 10% in all experiments.

## 4 CONCLUSION

In this paper, we introduced a novel multi-scale topology optimization framework using Voronoi microstructures. Our approach involves an offline homogenization process coupled with NN training to establish a continuous and differentiable mapping of microstructural geometric parameters to constitutive properties. Subsequently, we carried out multiscale optimization to minimize compliance subject to volume constraints.

Our numerical results illustrate that the proposed method offers significant computational advantages over concurrent homogenization, with minimal loss in accuracy. Additionally, we observe that Voronoi microstructures, along with parameters such as thickness anisotropy and orientation, expand the design space. Furthermore, considering neighboring microstructure cell sites during NN training facilitates macroscopic connectivity. Finally, training the NN with Cholesky factors ensures the positive definiteness of the constitutive matrix.

Future research avenues include extending the framework to encompass Voronoi structures found in natural systems, which often serve multiple functions. For example, in bone infills, pores act as conduits for transport while the material provides structural integrity. This could involve a multi-objective formulation integrating compliance and diffusivity to generate bone-like porous structures. In natural porous materials, the density of Voronoi cell sites varies, whereas in the present formulation, the number of cell sites in a region remains constant. Extending the framework to three dimensions is also a crucial area for future investigation. Additionally, the proposed framework focused on a singular class of microstructures derived from Turing patterns, but the potential for generating a broader spectrum of patterns exists through the application of reaction-diffusion equations [97].

## ACKNOWLEDGMENTS

The University of Wisconsin, Madison Graduate School supported this work.

## COMPLIANCE WITH ETHICAL STANDARDS

The authors declare that they have no conflict of interest.

## REPLICATION OF RESULTS

The Python code is available at [github.com/UW-ERSL/VoroTO](https://github.com/UW-ERSL/VoroTO), 11

## REFERENCES

- [1] Martin Philip Bendsoe and Ole Sigmund. *Topology optimization: theory, methods, and applications*. Springer Science & Business Media, 2013.
- [2] Ole Sigmund and Kurt Maute. Topology optimization approaches: A comparative review. *Structural and multi-disciplinary optimization*, 48(6):1031–1055, 2013.
- [3] Ronald F Gibson. A review of recent research on mechanics of multifunctional composite materials and structures. *Composite structures*, 92(12):2793–2810, 2010.
- [4] Franz Knoll and Thomas Vogel. *Design for robustness*, volume 11. IABSE, 2009.
- [5] Zhong Hu, Kaushik Thiyagarajan, Amrit Bhusal, Todd Letcher, Qi Hua Fan, Qiang Liu, and David Salem. Design of ultra-lightweight and high-strength cellular structural composites inspired by biomimetics. *Composites Part B: Engineering*, 121:108–121, 2017.
- [6] M Sadegh Ebrahimi, R Hashemi, and E Etemadi. In-plane energy absorption characteristics and mechanical properties of 3d printed novel hybrid cellular structures. *Journal of Materials Research and Technology*, 20:3616–3632, 2022.
- [7] Luis Cardoso, Susannah P Fritton, Gaffar Gailani, Mohammed Benalla, and Stephen C Cowin. Advances in assessment of bone porosity, permeability and interstitial fluid flow. *Journal of biomechanics*, 46(2):253–265, 2013.
- [8] Michael F Ashby and Lorna J Gibson. Cellular solids: structure and properties. *Press Syndicate of the University of Cambridge, Cambridge, UK*, pages 175–231, 1997.
- [9] Helge Klippstein, Hany Hassanin, Alejandro Diaz De Cerio Sanchez, Yahya Zweiri, and Lakmal Seneviratne. Additive manufacturing of porous structures for unmanned aerial vehicles applications. *Advanced Engineering Materials*, 20(9):1800290, 2018.
- [10] Shiqi Wu, Daming Chen, Guangdong Zhao, Yuan Cheng, Boqian Sun, Xiaojie Yan, Wenbo Han, Guiqing Chen, and Xinghong Zhang. Controllable synthesis of a robust sucrose-derived bio-carbon foam with 3d hierarchical porous structure for thermal insulation, flame retardancy and oil absorption. *Chemical Engineering Journal*, 434:134514, 2022.
- [11] Scott J Hollister. Porous scaffold design for tissue engineering. *Nature materials*, 4(7):518–524, 2005.
- [12] Young-Joon Seol, Dong Yong Park, Ju Young Park, Sung Won Kim, Seong Jin Park, and Dong-Woo Cho. A new method of fabricating robust freeform 3d ceramic scaffolds for bone tissue regeneration. *Biotechnology and Bioengineering*, 110(5):1444–1455, 2013.
- [13] Da Chen, Kang Gao, Jie Yang, and Lihai Zhang. Functionally graded porous structures: Analyses, performances, and applications—a review. *Thin-Walled Structures*, 191:111046, 2023.
- [14] Diplesh Gautam and Venkatesh KP Rao. Nondestructive evaluation of mechanical properties of femur bone. *Journal of Nondestructive Evaluation*, 40(1):22, 2021.

- [15] Chukwuzubelu Okenwa Ufodike, Mohammad Faisal Ahmed, and Grzegorz Dolzyk. Additively manufactured biomorphic cellular structures inspired by wood microstructure. *Journal of the Mechanical Behavior of Biomedical Materials*, 123:104729, 2021.
- [16] SR Jongerius and D Lentink. Structural analysis of a dragonfly wing. *Experimental Mechanics*, 50:1323–1334, 2010.
- [17] Haizum Aimi Zaharin, Ahmad Majdi Abdul Rani, Farooq I Azam, Turnad Lenggo Ginta, Nabihah Sallih, Azlan Ahmad, Nurul Azhani Yunus, and Tun Zainal Azni Zulkipli. Effect of unit cell type and pore size on porosity and mechanical behavior of additively manufactured ti6al4v scaffolds. *Materials*, 11(12):2402, 2018.
- [18] Christopher R Jacobs, Juan C Simo, Gary S Beaupre, and Dennis R Carter. Adaptive bone remodeling incorporating simultaneous density and anisotropy considerations. *Journal of biomechanics*, 30(6):603–613, 1997.
- [19] Jaejong Park, Alok Sutradhar, Jami J Shah, and Glaucio H Paulino. Design of complex bone internal structure using topology optimization with perimeter control. *Computers in biology and medicine*, 94:74–84, 2018.
- [20] Yohann Bala, Emmanuelle Lefèvre, Jean-Paul Roux, Cécile Baron, Philippe Lasaygues, Martine Pithioux, Valérie Kaftandjian, and Hélène Follet. Pore network microarchitecture influences human cortical bone elasticity during growth and aging. *Journal of the mechanical behavior of biomedical materials*, 63:164–173, 2016.
- [21] Ibrahim Goda, Jean-Francois Ganghoffer, Sławomir Czarnecki, Radosław Czubacki, and Paweł Wawruch. Topology optimization of bone using cubic material design and evolutionary methods based on internal remodeling. *Mechanics Research Communications*, 95:52–60, 2019.
- [22] Phong Cong Hong Nguyen, Youngdo Kim, and Young Choi. Lightweight design with metallic additively manufactured cellular structures. *Journal of Computational Design and Engineering*, 9(1):155–167, 2022.
- [23] Wahyudin P Syam, Wu Jianwei, Bo Zhao, Ian Maskery, Waiel Elmadih, and Richard Leach. Design and analysis of strut-based lattice structures for vibration isolation. *Precision Engineering*, 52:494–506, 2018.
- [24] Lorenzo Valdevit, Alan J Jacobsen, Julia R Greer, and William B Carter. Protocols for the optimal design of multifunctional cellular structures: from hypersonics to microarchitected materials. *Journal of the American Ceramic Society*, 94:s15–s34, 2011.
- [25] Gang Lei, PC Dong, ZS Wu, SH Gai, SY Mo, and Z Li. Multi-scale structures of porous media and the flow prediction. *Journal of Natural Gas Science and Engineering*, 21:986–992, 2014.
- [26] Jonàs Martínez, Jérémie Dumas, and Sylvain Lefebvre. Procedural voronoi foams for additive manufacturing. *ACM Transactions on Graphics (TOG)*, 35(4):1–12, 2016.
- [27] Guanjuan Wang, Lida Shen, Jianfeng Zhao, Huixin Liang, Deqiao Xie, Zongjun Tian, and Changjiang Wang. Design and compressive behavior of controllable irregular porous scaffolds: based on voronoi-tessellation and for additive manufacturing. *ACS biomaterials science & engineering*, 4(2):719–727, 2018.
- [28] Clément Audibert, Julien Chaves-Jacob, Jean-Marc Linares, and Quentin-Alexis Lopez. Bio-inspired method based on bone architecture to optimize the structure of mechanical workpieces. *Materials & Design*, 160:708–717, 2018.
- [29] Jianming Ying, Lin Lu, Lihao Tian, Xin Yan, and Baoquan Chen. Anisotropic porous structure modeling for 3d printed objects. *Computers & Graphics*, 70:157–164, 2018.
- [30] Jun Wu, Ole Sigmund, and Jeroen P Groen. Topology optimization of multi-scale structures: a review. *Structural and Multidisciplinary Optimization*, 63:1455–1480, 2021.
- [31] Rahul Kumar Padhy, Aaditya Chandrasekhar, and Krishnan Suresh. Fluto: Graded multi-scale topology optimization of large contact area fluid-flow devices using neural networks. *Engineering with Computers*, pages 1–17, 2023.
- [32] Rahul Kumar Padhy, Krishnan Suresh, and Aaditya Chandrasekhar. Tomas: Topology optimization of multiscale fluid devices using variational autoencoders and super-shapes. *arXiv preprint arXiv:2309.08435*, 2023.
- [33] Jun Wu, Christian Dick, and Rüdiger Westermann. A system for high-resolution topology optimization. *IEEE transactions on visualization and computer graphics*, 22(3):1195–1208, 2015.
- [34] Jun Wu, Weiming Wang, and Xifeng Gao. Design and optimization of conforming lattice structures. *IEEE transactions on visualization and computer graphics*, 27(1):43–56, 2019.
- [35] James K Guest. Imposing maximum length scale in topology optimization. *Structural and Multidisciplinary Optimization*, 37:463–473, 2009.
- [36] Suguang Dou. A projection approach for topology optimization of porous structures through implicit local volume control. *Structural and Multidisciplinary Optimization*, 62(2):835–850, 2020.
- [37] Sourav Das and Alok Sutradhar. Multi-physics topology optimization of functionally graded controllable porous structures: Application to heat dissipating problems. *Materials & Design*, 193:108775, 2020.
- [38] Zhi Zhao and Xiaoqia Shelly Zhang. Design of graded porous bone-like structures via a multi-material topology optimization approach. *Structural and Multidisciplinary Optimization*, 64:677–698, 2021.
- [39] Fan Feng, Shiyong Xiong, Ziyue Liu, Zangyueyang Xian, Yuqing Zhou, Hiroki Kobayashi, Atsushi Kawamoto, Tsuyoshi Nomura, and Bo Zhu. Cellular topology optimization on differentiable voronoi diagrams. *International Journal for Numerical Methods in Engineering*, 124(1):282–304, 2023.
- [40] Hongjia Lu, Ting-Uei Lee, Jiaming Ma, Da Chen, and Yi Min Xie. Designing 2d stochastic porous structures using topology optimisation. *Composite Structures*, 321:117305, 2023.

- [41] Yanfang Zhao, Guikai Guo, Xinyu Xie, and Wenjie Zuo. Concurrent multiscale topology optimization of hollow structures considering geometrical nonlinearity. *Engineering with Computers*, pages 1–18, 2023.
- [42] Martin P Bendsøe and Ole Sigmund. Material interpolation schemes in topology optimization. *Archive of applied mechanics*, 69:635–654, 1999.
- [43] Jun Yan, Qianqian Sui, Zhirui Fan, Zunyi Duan, and Tao Yu. Clustering-based multiscale topology optimization of thermo-elastic lattice structures. *Computational Mechanics*, 66:979–1002, 2020.
- [44] Hao Li, Zhen Luo, Nong Zhang, Liang Gao, and Terry Brown. Integrated design of cellular composites using a level-set topology optimization method. *Computer Methods in Applied Mechanics and Engineering*, 309:453–475, 2016.
- [45] Christian Schumacher, Steve Marschner, Markus Gross, and Bernhard Thomaszewski. Mechanical characterization of structured sheet materials. *ACM Transactions on Graphics (TOG)*, 37(4):1–15, 2018.
- [46] Davi Colli Tozoni, Jérémie Dumas, Zhongshi Jiang, Julian Panetta, Daniele Panozzo, and Denis Zorin. A low-parametric rhombic microstructure family for irregular lattices. *ACM Transactions on Graphics (TOG)*, 39(4):101–1, 2020.
- [47] Xin Yan, Cong Rao, Lin Lu, Andrei Sharf, Haisen Zhao, and Baoquan Chen. Strong 3d printing by tpms injection. *IEEE Transactions on Visualization and Computer Graphics*, 26(10):3037–3050, 2019.
- [48] Jiangbei Hu, Shengfa Wang, Baojun Li, Fengqi Li, Zhongxuan Luo, and Ligang Liu. Efficient representation and optimization for tpms-based porous structures. *IEEE Transactions on Visualization and Computer Graphics*, 28(7):2615–2627, 2020.
- [49] Ming Li, Jingqiao Hu, Wei Chen, Weipeng Kong, and Jin Huang. Explicit topology optimization of conforming voronoi foams. *arXiv preprint arXiv:2308.04001*, 2023.
- [50] Bruno Jetté, Vladimir Brailovski, Mathieu Dumas, Charles Simoneau, and Patrick Terriault. Femoral stem incorporating a diamond cubic lattice structure: Design, manufacture and testing. *Journal of the Mechanical Behavior of Biomedical Materials*, 77:58–72, 2018.
- [51] Farnaz Ghorbani, Dejian Li, Shuo Ni, Ying Zhou, and Baoqing Yu. 3d printing of acellular scaffolds for bone defect regeneration: A review. *Materials Today Communications*, 22:100979, 2020.
- [52] Long Chao, Yangdong He, Jiasen Gu, Deqiao Xie, Youwen Yang, Lida Shen, Guofeng Wu, Lin Wang, and Zongjun Tian. Evaluation of compressive and permeability behaviors of trabecular-like porous structure with mixed porosity based on mechanical topology. *Journal of Functional Biomaterials*, 14(1):28, 2023.
- [53] Hong-Yuan Lei, Jing-Rong Li, Zhi-Jia Xu, and Qing-Hui Wang. Parametric design of voronoi-based lattice porous structures. *Materials & Design*, 191:108607, 2020.
- [54] Lin Lu, Andrei Sharf, Haisen Zhao, Yuan Wei, Qingnan Fan, Xuelin Chen, Yann Savoye, Changhe Tu, Daniel Cohen-Or, and Baoquan Chen. Build-to-last: Strength to weight 3d printed objects. *ACM Transactions on Graphics (ToG)*, 33(4):1–10, 2014.
- [55] XY Kou and ST Tan. A simple and effective geometric representation for irregular porous structure modeling. *Computer-Aided Design*, 42(10):930–941, 2010.
- [56] Zhongren Wang, Lihao Tian, Xiaokang Liu, Andrei Sharf, and Lin Lu. Stochastic porous microstructures. *arXiv preprint arXiv:2305.09176*, 2023.
- [57] Filippo Cucinotta, Marcello Raffaele, and Fabio Salmeri. A stress-based topology optimization method by a voronoi tessellation additive manufacturing oriented. *The International Journal of Advanced Manufacturing Technology*, 103:1965–1975, 2019.
- [58] Lianxiong Chen, Ran Zhang, Xihua Chu, and Hui Liu. Multiscale design of graded stochastic cellular structures for the heat transfer problem. *Applied Sciences*, 13(7):4409, 2023.
- [59] Der-Tsai Lee and Robert L Drysdale, III. Generalization of voronoi diagrams in the plane. *SIAM Journal on Computing*, 10(1):73–87, 1981.
- [60] Howie Choset and Joel Burdick. Sensor-based exploration: The hierarchical generalized voronoi graph. *The International Journal of Robotics Research*, 19(2):96–125, 2000.
- [61] Kenneth E Hoff III, John Keyser, Ming Lin, Dinesh Manocha, and Tim Culver. Fast computation of generalized voronoi diagrams using graphics hardware. In *Proceedings of the 26th annual conference on Computer graphics and interactive techniques*, pages 277–286, 1999.
- [62] Elena Arseneva and Evanthia Papadopoulou. Randomized incremental construction for the hausdorff voronoi diagram revisited and extended. *Journal of Combinatorial Optimization*, 37:579–600, 2019.
- [63] Maxime Sainlot, Vincent Nivoliers, and Dominique Attali. Restricting voronoi diagrams to meshes using corner validation. In *Computer Graphics Forum*, volume 36, pages 81–91. Wiley Online Library, 2017.
- [64] Francois Labelle and Jonathan Richard Shewchuk. Anisotropic voronoi diagrams and guaranteed-quality anisotropic mesh generation. In *Proceedings of the nineteenth annual symposium on Computational geometry*, pages 191–200, 2003.
- [65] TFW Van Nuland, JAW Van Dommelen, and MGD Geers. An anisotropic voronoi algorithm for generating polycrystalline microstructures with preferred growth directions. *Computational Materials Science*, 186:109947, 2021.
- [66] Azwirman Gusrialdi, Sandra Hirche, Takeshi Hatanaka, and Masayuki Fujita. Voronoi based coverage control with anisotropic sensors. In *2008 American control conference*, pages 736–741. IEEE, 2008.
- [67] Travis E Oliphant et al. *Guide to numpy*, volume 1. Trelgol Publishing USA, 2006.
- [68] Erik Andreassen and Casper Schousboe Andreassen. How to determine composite material properties using numerical homogenization. *Computational Materials Science*, 83:488–495, 2014.

- [69] Charles F Jekel, Kenneth E Swartz, Daniel A White, Daniel A Tortorelli, and Seth E Watts. Neural network layers for prediction of positive definite elastic stiffness tensors. *arXiv preprint arXiv:2203.13938*, 2022.
- [70] Kurt Hornik, Maxwell Stinchcombe, and Halbert White. Multilayer feedforward networks are universal approximators. *Neural networks*, 2(5):359–366, 1989.
- [71] Tomonari Furukawa and Mark Hoffman. Accurate cyclic plastic analysis using a neural network material model. *Engineering Analysis with Boundary Elements*, 28(3):195–204, 2004.
- [72] Jörg F Unger and Carsten Könke. Neural networks as material models within a multiscale approach. *Computers & structures*, 87(19-20):1177–1186, 2009.
- [73] M Lefik, DP Boso, and BA Schrefler. Artificial neural networks in numerical modelling of composites. *Computer Methods in Applied Mechanics and Engineering*, 198(21-26):1785–1804, 2009.
- [74] Hou Man and Tomonari Furukawa. Neural network constitutive modelling for non-linear characterization of anisotropic materials. *International journal for numerical methods in engineering*, 85(8):939–957, 2011.
- [75] Guanghui Liang and K Chandrashekhara. Neural network based constitutive model for elastomeric foams. *Engineering structures*, 30(7):2002–2011, 2008.
- [76] V Papadopoulos, G Soimiris, DG Giovanis, and M Papadarakakis. A neural network-based surrogate model for carbon nanotubes with geometric nonlinearities. *Computer Methods in Applied Mechanics and Engineering*, 328:411–430, 2018.
- [77] Daniel A White, William J Arrighi, Jun Kudo, and Seth E Watts. Multiscale topology optimization using neural network surrogate models. *Computer Methods in Applied Mechanics and Engineering*, 346:1118–1135, 2019.
- [78] Liwei Wang, Yu-Chin Chan, Zhao Liu, Ping Zhu, and Wei Chen. Data-driven metamaterial design with laplace-beltrami spectrum as “shape-dna”. *Structural and multidisciplinary optimization*, 61:2613–2628, 2020.
- [79] Liwei Wang, Yu-Chin Chan, Faez Ahmed, Zhao Liu, Ping Zhu, and Wei Chen. Deep generative modeling for mechanistic-based learning and design of metamaterial systems. *Computer Methods in Applied Mechanics and Engineering*, 372:113377, 2020.
- [80] Zhaxylyk A Kudyshev, Alexander V Kildishev, Vladimir M Shalaev, and Alexandra Boltasseva. Machine-learning-assisted metasurface design for high-efficiency thermal emitter optimization. *Applied Physics Reviews*, 7(2), 2020.
- [81] Doksoo Lee, Wei Chen, Liwei Wang, Yu-Chin Chan, and Wei Chen. Data-driven design for metamaterials and multiscale systems: A review. *Advanced Materials*, 36(8):2305254, 2024.
- [82] Wei Ma, Feng Cheng, Yihao Xu, Qinlong Wen, and Yongmin Liu. Probabilistic representation and inverse design of metamaterials based on a deep generative model with semi-supervised learning strategy. *Advanced Materials*, 31(35):1901111, 2019.
- [83] Hunter T Kollmann, Diab W Abueidda, Seid Koric, Erman Guleryuz, and Nahil A Sobh. Deep learning for topology optimization of 2d metamaterials. *Materials & Design*, 196:109098, 2020.
- [84] Tianyu Zhao, Yiwen Li, Lei Zuo, and Kai Zhang. Machine-learning optimized method for regional control of sound fields. *Extreme Mechanics Letters*, 45:101297, 2021.
- [85] Tianshuo Qiu, Xin Shi, Jiafu Wang, Yongfeng Li, Shaobo Qu, Qiang Cheng, Tiejun Cui, and Sai Sui. Deep learning: a rapid and efficient route to automatic metasurface design. *Advanced Science*, 6(12):1900128, 2019.
- [86] Itzik Malkiel, Michael Mrejen, Achiya Nagler, Uri Arieli, Lior Wolf, and Haim Suchowski. Plasmonic nanostructure design and characterization via deep learning. *Light: Science & Applications*, 7(1):60, 2018.
- [87] Rebekka V Woldseth, Niels Aage, J Andreas Barentzen, and Ole Sigmund. On the use of artificial neural networks in topology optimisation. *Structural and Multidisciplinary Optimization*, 65(10):294, 2022.
- [88] Aaditya Chandrasekhar and Krishnan Suresh. Tounn: Topology optimization using neural networks. *Structural and Multidisciplinary Optimization*, 63:1135–1149, 2021.
- [89] Aaditya Chandrasekhar, Saketh Sridhara, and Krishnan Suresh. Graded multiscale topology optimization using neural networks. *Advances in Engineering Software*, 175:103359, 2023.
- [90] Jorge Nocedal and Stephen J Wright. *Numerical optimization*. Springer, 1999.
- [91] Diederik P Kingma and Jimmy Ba. Adam: A method for stochastic optimization. *arXiv preprint arXiv:1412.6980*, 2014.
- [92] Adam Paszke, Sam Gross, Francisco Massa, Adam Lerer, James Bradbury, Gregory Chanan, Trevor Killeen, Zeming Lin, Natalia Gimelshein, Luca Antiga, Alban Desmaison, Andreas Kopf, Edward Yang, Zachary DeVito, Martin Raison, Alykhan Tejani, Sasank Chilamkurthy, Benoit Steiner, Lu Fang, Junjie Bai, and Soumith Chintala. Pytorch: An imperative style, high-performance deep learning library. In *Advances in Neural Information Processing Systems 32*, pages 8024–8035. Curran Associates, Inc., 2019.
- [93] Aaditya Chandrasekhar, Saketh Sridhara, and Krishnan Suresh. Auto: a framework for automatic differentiation in topology optimization. *Structural and Multidisciplinary Optimization*, 64(6):4355–4365, 2021.
- [94] Ivan Vasilev, Daniel Slater, Gianmario Spacagna, Peter Roelants, and Valentino Zocca. *Python Deep Learning: Exploring deep learning techniques and neural network architectures with Pytorch, Keras, and TensorFlow*. Packt Publishing Ltd, 2019.
- [95] Erik Andreassen, Anders Clausen, Mattias Schevenels, Boyan S Lazarov, and Ole Sigmund. Efficient topology optimization in matlab using 88 lines of code. *Structural and Multidisciplinary Optimization*, 43:1–16, 2011.
- [96] Jun Wu, Niels Aage, Rüdiger Westermann, and Ole Sigmund. Infill optimization for additive manufacturing—approaching bone-like porous structures. *IEEE*

*transactions on visualization and computer graphics*,  
24(2):1127–1140, 2017.

- [97] Sarah N Hankins and Ray S Fertig III. Methodology for optimizing composite design via biological pattern generation mechanisms. *Materials & Design*, 197:109208, 2021.